Letters

Interphase LC Resonance and Stability Analysis of Series-Capacitor Buck Converters

Ping Wang, *Student Member, IEEE*, Daniel Zhou, *Student Member, IEEE*, Haoran Li, *Student Member, IEEE*, David M. Giuliano, Gregory Szczeszynski, Stephen Allen, and Minjie Chen, *Senior Member, IEEE*

***Abstract*—Hybrid switched capacitor power converters, such as the series-capacitor buck (SCB) converter, have intrinsic LC resonant dynamics that might influence its control stability and transient response. This letter presents a systematic approach to analyzing this intrinsic resonant behavior, which can be classified into output LC_o resonance and interphase LC_B resonance based on common-mode and differential-mode decomposition. The impacts of coupled inductors on the resonant amplitude, frequency, and settling time during a step line transient are analyzed. The influence of intrinsic resonance on control stability is clarified, providing guidance for controller design. A two-phase SCB prototype was built and tested with discrete and coupled inductors under different operating conditions. All the analyses are verified by simulation or experimental results.**

***Index Terms*—Averaged model, control, coupled inductor, LC resonance, multiphase converter, series-capacitor buck (SCB).**

I. Introduction

HYBRID switched-capacitor (SC) converters have been proved attractive for many applications [1], [2], [3], [4], [5], [6]. They leverage capacitors to achieve high power density and inductors to realize useful system functions such as soft charging and voltage regulation. In a hybrid SC converter, many capacitors and inductors may form a multiresonant system with sophisticated dynamics. This characteristic could significantly impact the controller design of hybrid SC converters, which has not been systematically investigated in literature. Using the series-capacitor buck (SCB) converter [5], [6], [7] as an example, this letter presents a systematic approach to analyzing the intrinsic LC resonance of hybrid SC converters and its impacts on control dynamics.

Manuscript received 22 October 2022; revised 4 December 2022 and 9 January 2023; accepted 24 January 2023. Date of publication 2 February 2023; date of current version 10 March 2023. This work was supported by pSemi Corporation. *(Corresponding author: Minjie Chen.)*

Ping Wang, Daniel Zhou, Haoran Li, and Minjie Chen are with the Department of Electrical and Computer Engineering and the Andlinger Center for Energy and the Environment, Princeton University, Princeton, NJ 08540 USA (e-mail: ping.wang@princeton.edu; dz8@princeton.edu; haoranli@princeton.edu; minjie@princeton.edu).

David M. Giuliano, Gregory Szczeszynski, and Stephen Allen are with the pSemi Corporation, San Diego, CA 92121 USA (e-mail: dgiuliano@psemi.com; gszczeszynski@psemi.com; sallen@psemi.com).

Color versions of one or more figures in this article are available at https://doi.org/10.1109/TPEL.2023.3241843.

Digital Object Identifier 10.1109/TPEL.2023.3241843

An SCB converter operates similar to a multiphase buck converter with inputs in series and outputs in parallel [5]. The reduced equivalent input voltage leads to: 1) extended duty ratio for high voltage conversion ratio; 2) reduced switch voltage stress and switching loss; 3) reduced inductor core loss; and 4) reduced current ripple. An inherent mutual balancing mechanism also exists, which can achieve automatic capacitor voltage balancing and inductor current sharing [8]. Previous large- and small-signal models of the SCB converter [9], [10], [11] only explain the overall converter dynamics, and interphase dynamics were not investigated. Shenoy et al. [8] unveiled the interphase LC resonance whose damping ratio is proportional to the conduction-path resistance. However, a well-designed high-efficiency converter with low conduction loss might result in an underdamped system with long settling time and large resonant amplitude. Models and design methods for describing and mitigating the interphase LC resonance are still needed.

This letter systematically analyzes the interphase LC resonance in SCB converters and provides comprehensive guidelines for controller design. The impact of coupled inductors on SCB interphase resonance is clarified. All the theoretical analyses are verified by simulation and experimental results.

II. Modeling and Analysis of Intrinsic Resonance

This section analyzes the intrinsic LC resonance by decomposing disturbance and its response into common-mode and differential-mode dynamics, streamlining the underlying mechanisms of SCB converter LC resonant behaviors. Fig. 1 shows the circuit topology and key operation waveforms of a two-phase SCB converter. The analysis below starts with using discrete inductors, and the impacts of coupled inductors are discussed in Section III. In the SCB topology, the blocking capacitor (C_B) functions as a dc voltage source with $v_{\text{in}}/2$ across it. Switch node voltages step between 0 and $v_{\text{in}}/2$, doubling the duty ratio compared to a regular buck. Two phases are typically interleaved, and C_B is charged and discharged by the inductor currents of the two phases alternatively as their high-side switches ($S_{1\sim2H}$) turn ON. Conduction-path resistances (including switch R_{ds}, capacitor equivalent series resistance, inductor winding resistance, etc.) are lumped into an effective resistance R_C in series with C_B. The large-signal average model of the two-phase SCB converter

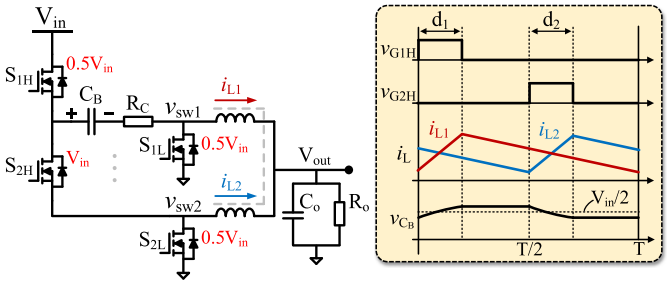

Fig. 1. Circuit topology and operation waveforms of an example two-phase SCB converter with discrete inductors. The maximum switch voltage stress is labeled in red. Coupled inductors can be utilized to replace the discrete ones, and phase number can be extended by stacking more SCB cells [10], [11], as indicated by the grey lines and grey dots.

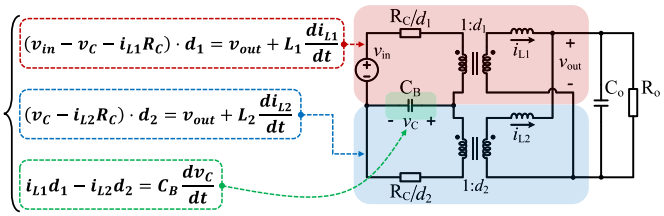

Fig. 2. Large-signal average model and its equivalent circuit model.

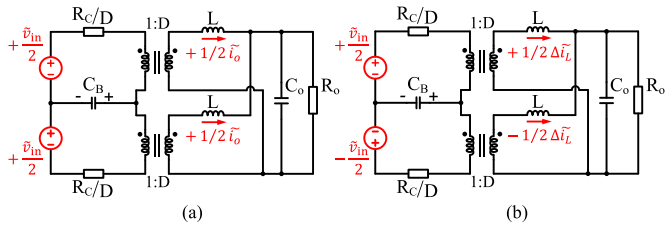

Fig. 3. Input voltage disturbance and its response decomposed into (a) common-mode dynamics and (b) differential-mode dynamics.

is described in Fig. 2 together with the modeling equations and their equivalent circuits.

The load transient dynamics of an SCB converter is similar to a multiphase buck converter and has been discussed in [11]. However, the line transient dynamics and their impacts on flying capacitor voltage and current sharing have not been systematically explored. The input voltage step change of a line transient results in blocking capacitor voltage variation and causes ringing and long settling time, which are the main focuses of this letter. Similar analysis methods can be applied to describe the responses to other perturbations, such as duty ratio change, unbalanced initial conditions, load transients, etc.

Assume $d_1 = d_2 = D$ and $L_1 = L_2 = L$. The input voltage perturbation $\tilde{v_{\text{in}}}$ can be decomposed into common mode $\{+\tilde{v_{\text{in}}}/2, +\tilde{v_{\text{in}}}/2\}$ and differential mode $\{+\tilde{v_{\text{in}}}/2, -\tilde{v_{\text{in}}}/2\}$ for the two phases, as illustrated in Fig. 3. The common-mode perturbations drive the two phases to change in the same way, while the differential-mode perturbations cause opposite variations on the two phases. The resulting differential inductor currents $\pm\Delta\tilde{i_L}/2$ are canceled at the output, so the common-mode current response is $+\tilde{i_o}/2$ for each inductor. The overall current response of each inductor is

$$\tilde{i_{L_1}} = \frac{1}{2}\tilde{i_o} + \frac{1}{2}\Delta\tilde{i_L}, \qquad \tilde{i_{L_2}} = \frac{1}{2}\tilde{i_o} - \frac{1}{2}\Delta\tilde{i_L}. \tag{1}$$

Apply state-space averaging, the $\tilde{v_{\text{in}}}$-to-$\tilde{i_o}$ transfer function is

$$G_{v_{\text{in}}i_o} = \frac{\tilde{i_o}}{\tilde{v_{\text{in}}}} = \frac{D}{2R_o + DR_C} \cdot \frac{\frac{s}{\omega_z}+1}{\frac{s^2}{\omega_{\text{nop}}^2} + \frac{s}{Q_{\text{op}}\omega_{\text{nop}}}+1}, \tag{2}$$

$$\omega_{\text{nop}} = \sqrt{\frac{2R_o+DR_C}{R_oC_oL}}, Q_{\text{op}} = \frac{\sqrt{\frac{R_oC_oL}{2R_o+DR_C}}}{L+R_CR_oC_oD}, \omega_z = \frac{1}{R_oC_o}. \tag{3}$$

Accordingly, the line transient $\tilde{v_{\text{in}}}$-to-$\tilde{v_o}$ transfer function is

$$G_{v_{\text{in}}v_o} = \frac{\tilde{v_o}}{\tilde{v_{\text{in}}}} = G_{v_{\text{in}}i_o} \cdot Z_o, \quad Z_o = \frac{R_o}{R_oC_os+1}. \tag{4}$$

Similarly, the $\tilde{v_{\text{in}}}$-to-$\Delta\tilde{i_L}$ transfer function is

$$G_{v_{\text{in}}\Delta i_L} = \frac{\Delta\tilde{i_L}}{\tilde{v_{\text{in}}}} = \frac{C_B}{2D} \cdot \frac{s}{\frac{s^2}{\omega_{\text{nip}}^2} + \frac{s}{Q_{\text{ip}}\omega_{\text{nip}}}+1}, \tag{5}$$

$$\omega_{\text{nip}} = D\sqrt{\frac{2}{LC_B}}, \quad Q_{\text{ip}} = \frac{1}{R_C}\sqrt{\frac{2L}{C_B}}. \tag{6}$$

It can be seen from (2) and (5) that there exist two types of intrinsic LC resonances in SCB converter dynamic responses.

1) Output LC_o resonance with ω_{nop} and Q_{op}: Higher R_o leads to a higher Q_{op} and lower damping ratio.
2) Interphase LC_B resonance with ω_{nip} and Q_{ip}: Higher R_C results in a lower Q_{ip} and higher damping ratio.

Dynamic responses of common-mode variables (e.g., $\tilde{i_o}$ and $\tilde{v_o}$) will only see the output LC_o resonant pole and their associated transfer functions (e.g., $G_{v_{\text{in}}i_o}$, $G_{v_{\text{in}}v_o}$, and G_{dv_o}) are the same as of a regular two-phase buck. Contrarily, responses of differential-mode variables (e.g., $\Delta\tilde{i_L}$ and $\tilde{v_C}$) will only see the interphase LC_B resonant pole, whose transfer functions (e.g., $G_{v_{\text{in}}v_c}$, $G_{v_{\text{in}}\Delta i_L}$, and $G_{\Delta d\Delta i_L}$) are different from the buck converter. According to (1), responses of $\tilde{i_{L_1}}/\tilde{i_{L_2}}$ contain both common-mode and differential-mode dynamics and will see both output LC_o and interphase LC_B resonant poles. The $\tilde{v_{\text{in}}}$-to-$\tilde{i_{L_1}}/\tilde{i_{L_2}}$ transfer functions can be obtained by combining $G_{v_{\text{in}}i_o}$ and $G_{v_{\text{in}}\Delta i_L}$. The same analysis approach and conclusions also apply to SCB converters with higher number of phases.

For a general M-phase SCB converter, transfer functions can be calculated based on state-space modeling as summarized in the Appendix. A more intuitive way of deriving the response to a perturbation is by superposing the responses to its common-mode and differential-mode components. Fig. 4(a) plots the small-signal average model of an M-phase SCB converter and its equivalent circuits seen by common-mode and differential-mode perturbations individually. Denote the effective perturbations applied to each phase as $\tilde{v_1} \sim \tilde{v_M}$, which can represent input voltage or converted duty ratio perturbations (e.g., $\tilde{v_1} = \tilde{v_{\text{in}}}$, $\tilde{v_{2\sim M}} = 0$ representing the input voltage perturbation). As shown in Fig. 4(a), the common-mode perturbation component $\tilde{v_{\text{cm}}}$ ($\tilde{v_{\text{cm}}} = \Sigma_{k=1}^{M}\tilde{v_k}/M$) is effectively applied to an output LC_oR_o network with the resonant frequency of

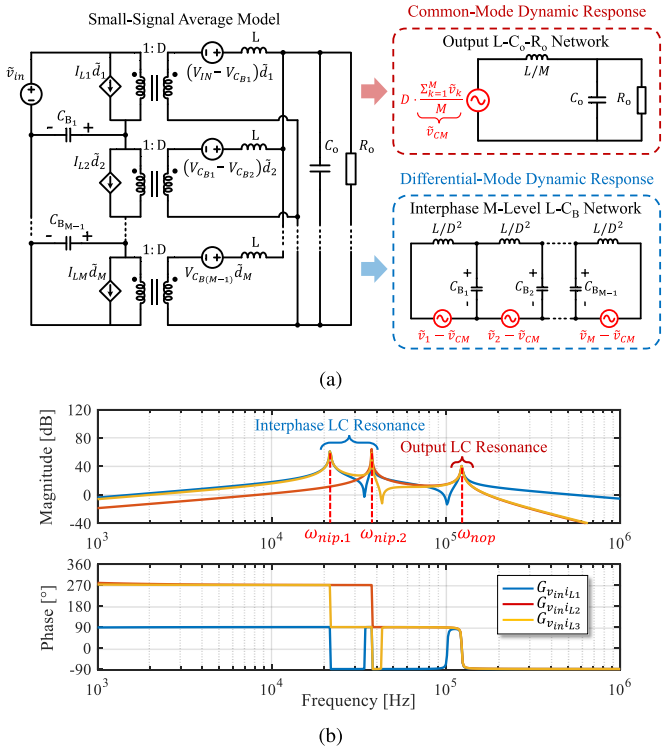

Fig. 4. (a) Response decomposition of common-mode and differential-mode dynamics for a general M-phase SCB converter (R_C is ignored here). (b) $\tilde{v}_{\text{in}}$-to-$\tilde{i}_L$ transfer functions of an example three-phase SCB converter, where $L = 50$ nH, $C_{B1,2} = 30$ μF, $C_o = 100$ μF, $R_o = 1$ Ω, and $D = 1/6$. All the magnitude dB values are calculated based on SI units in this letter.

$\omega_{\text{nop}} = \sqrt{\frac{M}{LC_o}}$. Same for the output load transient that contains only common-mode perturbation component.

As for differential-mode perturbations, the incurred variations are canceled at the output, so the output terminals are effectively shorted in the small-signal average model, resulting in an equivalent M-level LC_B ladder network. Transfer function for this LC ladder circuit can be determined by using DFFz triangles [12], which contains up to $M-1$ resonant poles (assume $C_{B.k}$ are identical)

$$\omega_{\text{nip}.k} = \frac{2D}{\sqrt{LC_B}} \sin\left(\frac{k\pi}{2M}\right), \quad k = 1, \ldots, M-1. \tag{7}$$

Lumping the common-mode and differential-mode dynamic responses yields the overall response. Fig. 4(b) shows the $\tilde{v}_{\text{in}}$-to-$\tilde{i}_L$ transfer functions of an example three-phase SCB converter, which contains two interphase LC_B resonant poles and one output LC_o resonant pole, as expected.

III. Impacts of Coupled Inductors

Coupled inductors that exhibit different inductances to common-mode and differential-mode excitations can improve inductor current sharing and capacitor voltage balancing for multiphase hybrid SC magnetic topologies [13], [14]. This section discusses the impacts of coupled inductors on intrinsic resonance of the SCB converter. Table I lists the parameters of an example two-phase SCB for all calculations and simulations

TABLE I
Parameters of a Two-Phase SCB Converter

V_{in}	V_{out}	f_{sw}	C_B	R_C	L_k	C_o	R_o
12V	1V	1MHz	30μF	3mΩ	50nH	100μF	20mΩ

* Parameters are the same for all calculations and simulations in Sections III and IV, unless otherwise specified.

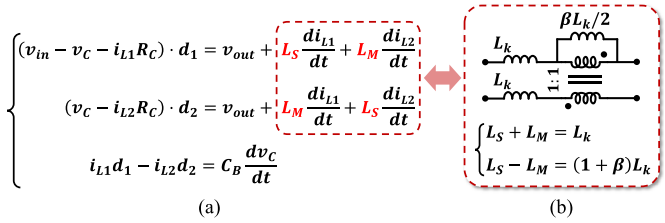

Fig. 5. (a) Large-signal average model of using coupled inductors. (b) Equivalent circuit and parameter conversion for a two-phase coupled inductor.

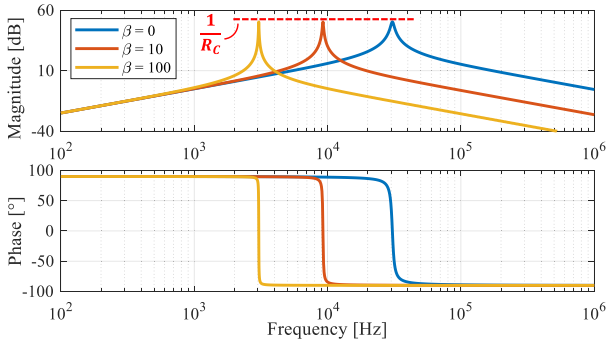

Fig. 6. Bode plots of $G_{v_{\text{in}}\Delta i_L}$ with different coupling coefficients.

in Sections III and IV, unless otherwise specified. Fig. 5 shows the large-signal average model with coupled inductors. L_S and L_M are self-inductance and mutual inductance in the inductance matrix, respectively, and L_k and β are effective leakage inductance and coupling coefficient, respectively, as defined in [14] and [15]. A higher β indicates higher coupling coefficient for the coupled inductor. When using coupled inductors, transfer functions $G_{v_{\text{in}}i_o}$, $G_{v_{\text{in}}v_o}$, and $G_{v_{\text{in}}\Delta i_L}$ have the same expressions as in (2)–(6) except that ω_n and Q are changed to

$$\omega_{\text{nop}} = \sqrt{\frac{2R_o + DR_C}{R_o C_o L_k}}, \quad Q_{\text{op}} = \frac{\sqrt{\frac{R_o C_o L_k}{2R_o + DR_C}}}{L_k + R_C R_o C_o D}, \tag{8}$$

$$\omega_{\text{nip}} = D\sqrt{\frac{2}{(1+\beta)L_k C_B}}, \quad Q_{\text{ip}} = \frac{1}{R_C}\sqrt{\frac{2(1+\beta)L_k}{C_B}}. \tag{9}$$

Accordingly, common-mode or output dynamics will see a small inductance L_k, while the differential-mode or interphase dynamics will see a large inductance $(1+\beta)L_k$. If L_k is fixed (i.e., under the same transient speed), β will only influence differential-mode dynamics. As shown in Fig. 6, a larger coefficient β results in a lower interphase resonant frequency ω_{nip} and a higher quality factor Q_{ip}, but the gain at resonance remains unchanged as $1/R_C$. When β increases, higher Q with narrower high-gain bandwidth may benefit the line transient response,

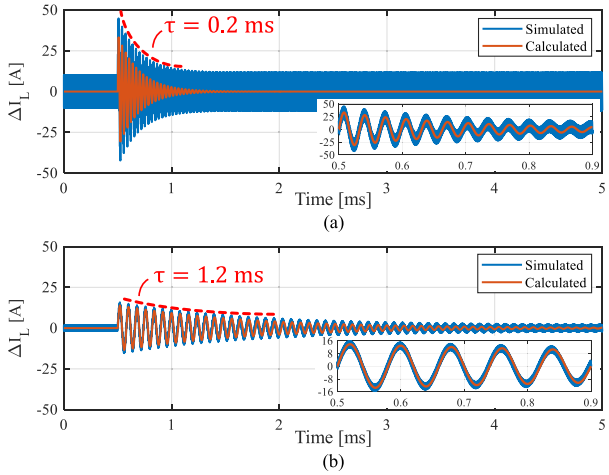

Fig. 7. Simulated and calculated Δi_L during a line transient (v_{in} steps from 12 to 14 V) when using (a) discrete inductors ($\beta = 0$) : and (b) a coupled inductor ($\beta = 5$).

since a v_{in} step change contains multiple frequency components. In the frequency domain, a v_{in} step change is $\tilde{v_{\text{in}}} = \frac{U}{s}$ (U is the step amplitude), and the Δi_L response is $\Delta\tilde{i_L} = G_{v_{\text{in}}\Delta i_L} \cdot \frac{U}{s}$. Accordingly, its time-domain response is

$$\Delta i_L(t) = \mathcal{L}^{-1}\left\{G_{v_{\text{in}}\Delta i_L} \cdot \frac{U}{s}\right\} = A \cdot e^{-\sigma t}\sin(\omega_d t) \tag{10}$$

$$A = 2U\sqrt{\frac{C_B}{8(1+\beta)L_k - R_C^2 C_B}},\quad \sigma = \frac{DR_C}{2(1+\beta)L_k},$$

$$\omega_d = \frac{D}{2(1+\beta)L_k}\sqrt{\frac{8(1+\beta)L_k - R_C^2 C_B}{C_B}}. \tag{11}$$

Fig. 7 shows the simulated and calculated responses of Δi_L to an input voltage step change, in which the calculated results match well with the simulated ones, validating the analysis. The 2% settling time of Δi_L envelop is $t_s = \frac{4}{\sigma}$. Fig. 7 also indicates that using coupled inductors can effectively suppress the amplitude of interphase resonance for SCB converters with the tradeoff of increased settling time. This feature fundamentally comes from larger effective inductance $(1+\beta)L_k$ for differential-mode (i.e., interphase) dynamics. The relationship between the resonant Δi_L amplitudes and the 2% settling time (t_s) during a unit v_{in} step change are plotted in Fig. 8, which implies that: 1) larger C_B leads to smaller capacitor voltage ripple but results in larger resonant current amplitude; and 2) as t_s increases, the resonant current amplitude decreases.

IV. Influence on Control Stability

This section explains the impacts of intrinsic resonance on control stability when the SCB converter is controlled in voltage mode. A typical multiphase PWM voltage-mode controller generates identical duty ratio command for each phase by sensing $\tilde{v_o}$. Fig. 9 plots its block diagram. H_s and A_c are transfer functions for sampling and compensation networks, respectively. As implied by the equivalent circuit model in Fig. 2, the identical duty commands will cause common-mode variations (e.g., $\tilde{i_o}$),

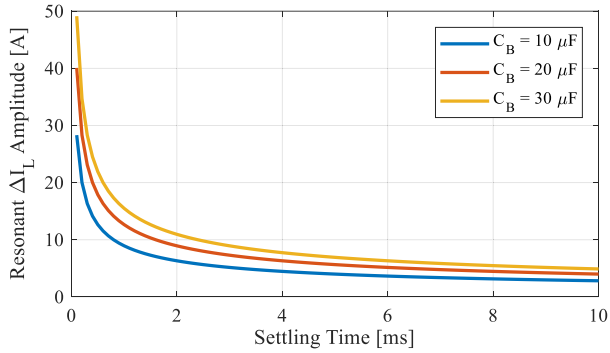

Fig. 8. Resonant ΔI_L amplitude versus 2% settling time (t_s) during a unit v_{in} step change. ($D = \frac{1}{6}$ and $R_C = 3$ mΩ.)

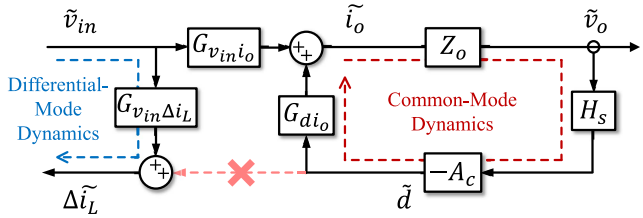

Fig. 9. Block diagram of an SCB converter with typical voltage-mode control.

but will not incur differential-mode variations (e.g., $\Delta\tilde{i_L}$ and $\tilde{v_c}$). Substituting $d_1 = d_2 = D + \tilde{d}$ into the average model, the $\tilde{d}$-to-$\tilde{i_o}$ transfer function is

$$G_{di_o} = \frac{\tilde{i_o}}{\tilde{d}} = \frac{V_{\text{in}} - I_o R_C}{2R_o + DR_C} \cdot \frac{\frac{s}{\omega_z} + 1}{\frac{s^2}{\omega_{\text{nop}}^2} + \frac{s}{Q_{\text{op}}\omega_{\text{nop}}} + 1}, \tag{12}$$

where ω_z, ω_{nop}, and Q_{op} are for output LC_oR_o network and are the same as in (3) or (8). $G_{dv_o} = G_{di_o} \cdot Z_o$. Since the sensed $\tilde{v_o}$ is also a common-mode variable, the overall feedback loop only senses and affects common-mode dynamics; it will not be influenced by or have impacts on differential-mode dynamics. Consequently, interphase LC_B resonance does not affect control stability; stable loop design only needs to consider the output LC_o resonance, which is the same as a multiphase buck. Similar conclusions can be drawn for other control methods that sense the common-mode dynamics and generate identical commands for all the phases.

Fig. 10 shows the simulated open-loop and closed-loop transfer functions for an example SCB converter with a typical voltage-mode controller. Denote the loop gain as $T = Z_o \cdot H_s \cdot A_c \cdot G_{di_o}$. A smaller L_k results in a larger ω_{nop} in G_{di_o}, allowing to design higher loop-gain bandwidth to achieve faster transient speed. Responses of $\tilde{i_o}$ and $\tilde{v_o}$ are involved in the loop, so the closed loop gains of $G_{v_{\text{in}}i_o}$ and $G_{v_{\text{in}}v_o}$ are greatly suppressed; responses of $\Delta\tilde{i_L}$ are not affected by the loop, so the closed-loop gain of $G_{v_{\text{in}}\Delta i_L}$ is unchanged:

$$(G_{v_{\text{in}}i_o})^{\text{CL}} = \frac{G_{v_{\text{in}}i_o}}{1+T},\quad (G_{v_{\text{in}}v_o})^{\text{CL}} = \frac{G_{v_{\text{in}}v_o}}{1+T},$$
$$(G_{v_{\text{in}}\Delta i_L})^{\text{CL}} = G_{v_{\text{in}}\Delta i_L}. \tag{13}$$

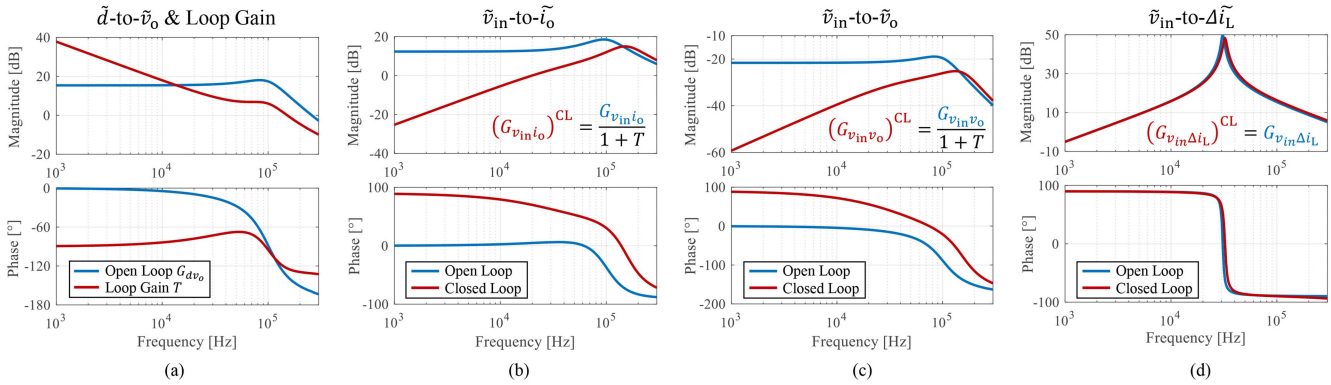

Fig. 10. Open- and closed-loop transfer functions in SPICE simulations. (a) Open loop G_{dv_o} and loop gain. (b) $G_{v_{in}i_o}$. (c) $G_{v_{in}v_o}$. (d) $G_{v_{in}\Delta i_L}$. ($\beta = 0$)

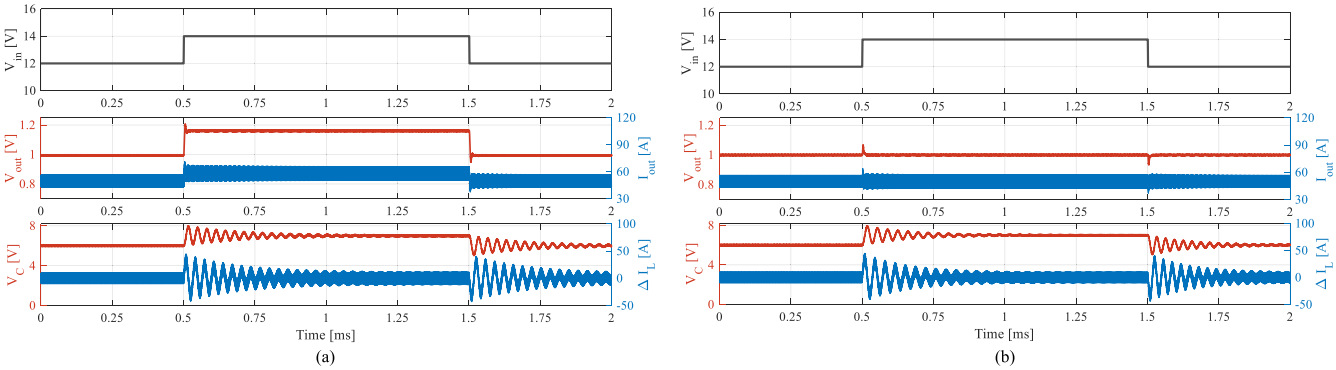

Fig. 11. Simulated voltage and current responses to a line transient (V_{in} = 12 V→14 V→12 V) in the case of (a) open loop and (b) closed loop. ($\beta = 0$)

Equation (13) indicates that the voltage-mode control loop can restrain the output variation, but it cannot suppress the interphase resonance. Therefore, as shown in Fig. 11, while the output voltage and current are effectively controlled to maintain stable against a line transient, the resonance of v_c and Δi_L are still left underdamped with high resonance amplitude and long settling time.

Actively controlling Δi_L resonance with unequal duty ratios will face more complicate $\Delta\tilde{d}$-to-$\Delta\tilde{i_L}$ dynamics than that of the multiphase buck. Substituting $d_1 = D + \frac{1}{2}\Delta\tilde{d}$ and $d_2 = D - \frac{1}{2}\Delta\tilde{d}$ into the average model, the $\Delta\tilde{d}$-to-$\Delta\tilde{i_L}$ transfer function can be obtained

$$G_{\Delta d\Delta i_L} = \frac{\Delta\tilde{i_L}}{\Delta\tilde{d}} = -\frac{I_o}{2D}\cdot\frac{1-\frac{s}{\omega_{z_{\rm rhp}}}}{\frac{s^2}{\omega_{\rm nip}^2}+\frac{s}{Q_{\rm ip}\omega_{\rm nip}}+1}, \tag{14}$$

where $\omega_{\rm nip}$ and $Q_{\rm ip}$ are the same as in (6) or (9), and the right-half-plane zero is $\omega_{z_{\rm rhp}} = \frac{2I_oD}{(V_{\rm in}-I_oR_C)C_B}$. Fig. 12 plots the bode plots of $G_{\Delta d\Delta i_L}$ under different load conditions. The right-half-plane zero together with the interphase resonant poles results in a 270° phase reduction. As I_o decreases, both $\omega_{z_{\rm rhp}}$ and the dc gain will reduce toward zero. The dc gain might even flip the sign due to nonlinear factors at very light load. All these issues could bring challenges to the active control of Δi_L and need to be properly handled.

An alternative way of actively suppressing interphase resonance is to control v_c resonance. Similar to (14), the $\Delta\tilde{d}$-to-v_c

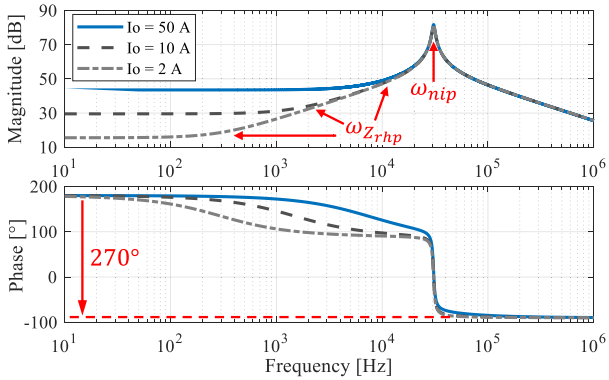

Fig. 12. Bode plots of $G_{\Delta d\Delta i_L}$ under different load conditions.

transfer function can be derived as

$$G_{\Delta dv_c} = \frac{\tilde{v_c}}{\Delta\tilde{d}} = \frac{V_{\rm in}}{4D}\cdot\frac{1+\frac{s}{\omega_{z_c}}}{\frac{s^2}{\omega_{\rm nip}^2}+\frac{s}{Q_{\rm ip}\omega_{\rm nip}}+1}, \tag{15}$$

where $\omega_{\rm nip}$ and $Q_{\rm ip}$ are the same as in (6) or (9), and $\omega_{z_c} = \frac{DV_{\rm in}}{I_o(1+\beta)L_k}$. The dc gain of $G_{\Delta dv_c}$ can describe the impacts of unequal duty ratios on the unbalanced value of C_B steady-state voltage, which could also be caused by resistance variation between phases [8], phase shift error [13], and source impedance [16]. Fig. 13 shows the bode plots of $G_{\Delta dv_c}$, in which there is no right-half-plane zero and the maximum phase

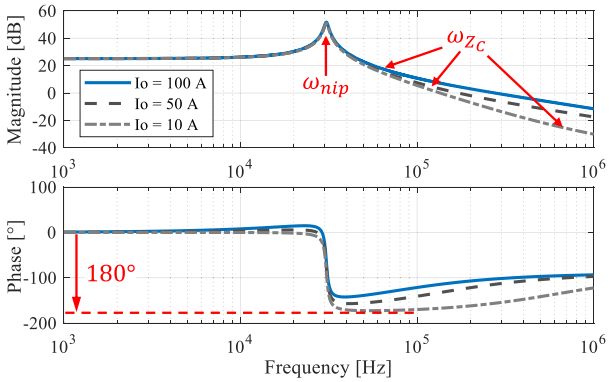

Fig. 13. Bode plots of $G_{\Delta dv_c}$ under different load conditions.

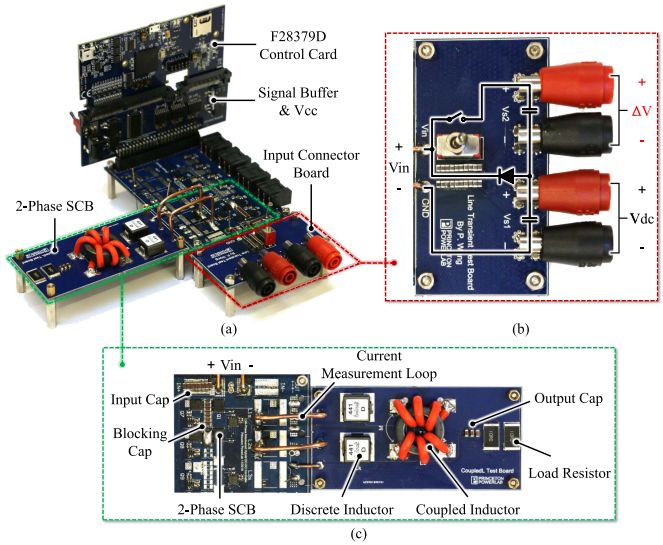

Fig. 14. Experimental hardware setup. (a) Overall prototype. (b) Line transient input connector board. (c) Annotated two-phase SCB converter.

reduction is 180° under all load conditions, making it attractive to design a C_B voltage control loop for suppressing the interphase LC_B resonance.

V. Experimental Results

To verify the analysis, a two-phase SCB converter was built and tested with both discrete and coupled inductors. Fig. 14 shows the overall hardware prototype. An input connector board [see Fig. 14(b)] for the line transient test is designed, which can provide an input voltage step change by switching in a second voltage source Δv. Fig. 14(c) annotates the tested SCB converter. Key component parameters are tabulated in Table II. The prototype designed herein is to verify the theoretical analysis. Demonstrating high efficiency or power density is out of the scope of this letter. Following experiments are performed as the SCB prototype converts 6 to 0.5 V and switches at 300 kHz, unless otherwise specified.

Fig. 15 shows key operation waveforms of the SCB converter. The discrete design contains two stand-alone inductors, while the coupled case contains both stand-alone inductors and a toroidal coupled inductor. This setup ensures that the discrete and coupled cases have roughly the same leakage inductance (or transient di/dt). As shown in Fig. 15, the coupled inductor can greatly reduce the current ripple while having roughly the same transient speed as the discrete ones.

TABLE II
Bill-of-Material of the Two-Phase SCB Converter

Device and Symbol	Component Description
Switches, $S_{1H/L} \sim S_{2H/L}$	Infineon BSC009NE2LS5I
Blocking capacitor, C_B	KEMET, X7R, 50 V, 4.7 μF × 7
Output capacitor, C_o	KEMET, X7R, 25 V, 10 μF × 3
Output resistor, R_o	TE, thick film, 10 Ω × 2
Discrete inductor	Coilcraft SLC1480-441
Coupled inductor	Toroidal 22/14/6.4, turns ratio 3:3 Core material: Fair-Rite 79

* Effective capacitances: C_B(@ 3 V) = 32.2 μF; C_o(@ 0.5 V) = 30 μF.

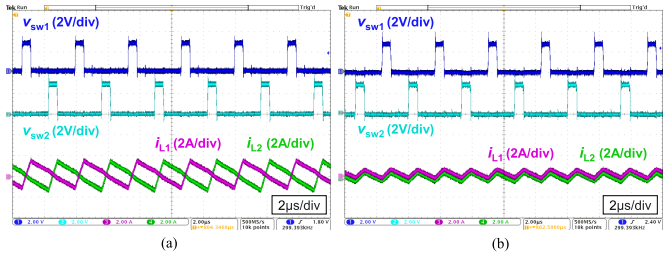

Fig. 15. Switch node voltages and inductor currents (as defined in Fig. 1) for (a) the discrete inductor setup ($L_k = 505$ nH) and (b) the coupled inductor setup ($L_k = 560$ nH, $L_M = 7.43$ μH, and $\beta = 27$). L_k and β are measured for the full path from the switch node to the output.

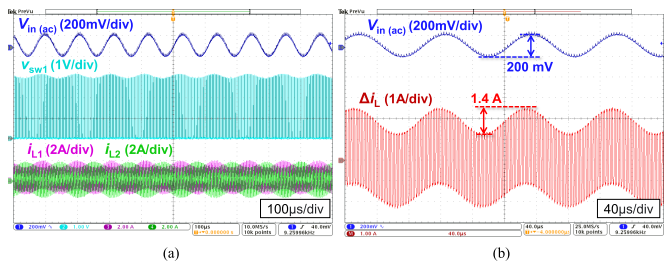

Fig. 16. Responses of (a) switch node voltage v_{sw1} and inductor currents $i_{L1\sim2}$ and (b) inductor current difference Δi_L to the input voltage perturbation at the interphase resonant frequency $\omega_{nip} = 9.26$ kHz (for the discrete design).

With measured L_k and C_B, the interphase resonant frequency for the discrete design can be obtained as 9.26 kHz. Fig. 16 shows the responses of inductor currents and switch node voltage to a 9.26-kHz input voltage perturbation. At the resonant frequency, a small input voltage perturbation (200-mV $v_{in(pp)}$) may incur large resonant inductor currents (1.4-A $\Delta I_{L(pp)}$), which are oppositely distributed on the two inductors. Accordingly, the equivalent resistance $R_C = 1/7$ Ω. In practical designs with optimized conduction losses and smaller R_C, the resonant issue will get even worse. Thus, proper input filters and control methods are needed to prevent interphase LC_B resonances from causing damages to the devices.

Figs. 17 and 18 show the simulated and the experimental waveforms of the inductor current response to a line transient

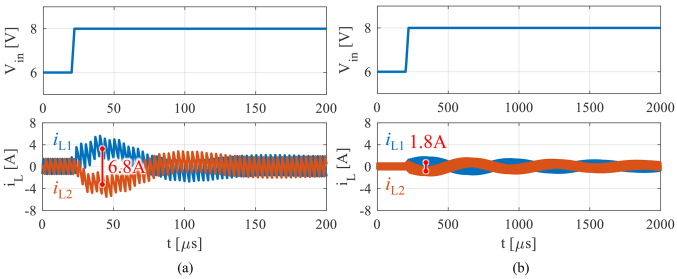

Fig. 17. Simulated line transient responses when using (a) discrete inductors and (b) the coupled inductor. V_{in} steps from 6 to 8 V. Simulations are based on $R_C = 1/7\ \Omega$ and other prototype circuit parameters.

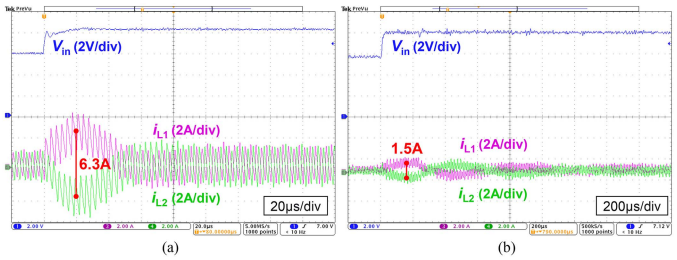

Fig. 18. Line transient test when using (a) discrete inductors and (b) the coupled inductor. V_{in} steps from 6 to 8 V. The experimental waveforms match well with the simulation waveforms in Fig. 17.

when using different inductor setups. The simulated and experimental results have a good match. Compared with discrete inductors, the coupled inductor can effectively reduce $\Delta i_{L,\max}$ at the cost of increased settling time as expected. Based on (10), the calculated $\Delta i_{L,\max}$ at the first resonant peak for the two inductor setups are 6.2 and 1.8 A. The discrepancy between calculated, simulated, and experimental results is mainly due to component value mismatch as well as the impacts of output LC_o resonance.

VI. Conclusion

This letter presented a systematic approach of analyzing the intrinsic LC resonant behavior in SCB converters. By decomposing disturbance and its response into common-mode and differential-mode dynamics, the intrinsic resonant behavior can be classified into output LC_o resonance and interphase LC_B resonance. Similar analysis approach can be extended to higher number of phases, enabling a more intuitive understanding of SCB converter transient and balancing behaviors. The impacts of coupled inductors were analyzed, indicating that higher coupling coefficient results in smaller resonant amplitude and lower resonant frequency with longer settling time. Comprehensive guidelines for designing a controller that cover both line transients and interphase resonance were provided. All the analyses were verified by simulation or experimental results.

Appendix
State-Space Model of an M-Phase SCB Converter

An M-phase SCB converter contains M inductors, $M-1$ blocking capacitors, and one output capacitor, so there are $2M$ state variables. Select the state vector as $\mathbf{x} = [i_{L_1}, i_{L_2}, \ldots, i_{L_M} \,\vdots\, v_{C_1}, v_{C_2}, \ldots, v_{C_M-1}, v_o]^T$, the input vector as $\mathbf{u} = [v_{\text{in}}]$, and the output vector as $\mathbf{y} = [i_{L_1}, i_{L_2}, \ldots, i_{L_M} \,\vdots\, i_o, v_o]^T$. Applying switching-cycle averaging, the state-space model can be obtained as

$$\dot{\mathbf{x}} = \mathbf{A}\mathbf{x} + \mathbf{B}\mathbf{u}, \tag{16}$$

$$\mathbf{y} = \mathbf{E}\mathbf{x}, \tag{17}$$

where the coefficient matrix $\mathbf{A}$ is

$$\mathbf{A} = \left[\begin{array}{c|c} \mathbf{0_{M\times M}} & \mathbf{A_{12}} \\ \hline \mathbf{A_{21}} & \mathbf{A_{22}} \end{array}\right], \tag{18}$$

and the block matrices $\mathbf{A_{12}}$, $\mathbf{A_{21}}$, and $\mathbf{A_{22}}$ are

$$\mathbf{A_{12}} = \begin{bmatrix} \frac{-D}{L_1} & 0 & \cdots & 0 & \frac{-1}{L_1} \\ \frac{D}{L_2} & \frac{-D}{L_2} & & \vdots & \frac{-1}{L_2} \\ 0 & \ddots & \ddots & 0 & \vdots \\ \vdots & & \frac{D}{L_{M-1}} & \frac{-D}{L_{M-1}} & \frac{-1}{L_{M-1}} \\ 0 & \cdots & 0 & \frac{D}{L_M} & \frac{-1}{L_M} \end{bmatrix}, \tag{19}$$

$$\mathbf{A_{21}} = \begin{bmatrix} \frac{D}{C_{B_1}} & \frac{-D}{C_{B_1}} & 0 & \cdots & 0 \\ 0 & \frac{D}{C_{B_2}} & \frac{-D}{C_{B_2}} & & \vdots \\ \vdots & & \ddots & \ddots & 0 \\ 0 & \cdots & 0 & \frac{D}{C_{B_{M-1}}} & \frac{-D}{C_{B_{M-1}}} \\ \frac{1}{C_o} & \frac{1}{C_o} & \cdots & \frac{1}{C_o} & \frac{1}{C_o} \end{bmatrix}, \tag{20}$$

$$\mathbf{A_{22}} = \begin{bmatrix} \mathbf{0_{M-1\times M-1}} & \mathbf{0_{M-1\times 1}} \\ \mathbf{0_{1\times M-1}} & -\frac{1}{C_o R_o} \end{bmatrix}. \tag{21}$$

The coefficient matrices $\mathbf{B}$ and $\mathbf{E}$ are

$$\mathbf{B} = \begin{bmatrix} \frac{D}{L_1} & \mathbf{0_{1\times 2M-1}} \end{bmatrix}^T, \tag{22}$$

$$\mathbf{E} = \left[\begin{array}{c|c} \mathbf{I_{M\times M}} & \mathbf{0_{M\times M}} \\ \hline 1, 1, \ldots, 1 & 0, 0, \ldots, 0 \\ 0, 0, \ldots, 0 & 0, \ldots, 0, 1 \end{array}\right]. \tag{23}$$

Accordingly, the transfer functions can be derived as

$$G_{v_{\text{in}} i_{L_k}} = \frac{\tilde{i_{L_k}}}{\tilde{v_{\text{in}}}} = (\mathbf{E})^{\text{row k}} \cdot (s\mathbf{I} - \mathbf{A})^{-1}\mathbf{B}, \tag{24}$$

$$G_{v_{\text{in}} i_o} = \frac{\tilde{i_o}}{\tilde{v_{\text{in}}}} = (\mathbf{E})^{\text{row M+1}} \cdot (s\mathbf{I} - \mathbf{A})^{-1}\mathbf{B}, \tag{25}$$

$$G_{v_{\text{in}} v_o} = \frac{\tilde{v_o}}{\tilde{v_{\text{in}}}} = (\mathbf{E})^{\text{row M+2}} \cdot (s\mathbf{I} - \mathbf{A})^{-1}\mathbf{B}. \tag{26}$$

References

[1] D. Reusch, F. C. Lee, and M. Xu, "Three level buck converter with control and soft startup," in *Proc. IEEE Energy Convers. Congr. Expo.*, 2009, pp. 31–35.

[2] J. S. Rentmeister and J. T. Stauth, "A 48V:2V flying capacitor multilevel converter using current-limit control for flying capacitor balance," in *Proc. IEEE Appl. Power Electron. Conf. Expo.*, 2017, pp. 367–372.

[3] Z. Ye, Y. Lei, and R. C. N. Pilawa-Podgurski, "The cascaded resonant converter: A hybrid switched-capacitor topology with high power density and efficiency," *IEEE Trans. Power Electron.*, vol. 35, no. 5, pp. 4946–4958, May 2020.

[4] S. Jiang, S. Saggini, C. Nan, X. Li, C. Chung, and M. Yazdani, "Switched tank converters," *IEEE Trans. Power Electron.*, vol. 34, no. 6, pp. 5048–5062, Jun. 2019.

[5] P. S. Shenoy, M. Amaro, J. Morroni, and D. Freeman, "Comparison of a buck converter and a series-capacitor buck converter for high-frequency, high-conversion-ratio voltage regulators," *IEEE Trans. Power Electron.*, vol. 31, no. 10, pp. 7006–7015, Oct. 2016.

[6] K. Nishijima, K. Harada, T. Nakano, T. Nabeshima, and T. Sato, "Analysis of double step-down two-phase buck converter for VRM," in *Proc. IEEE Telecommun. Energy Conf.*, 2005, pp. 497–502.

[7] J. Yungtaek, M. M. Jovanovic, and Y. Panov, "Multiphase buck converters with extended duty cycle," in *Proc. IEEE Appl. Power Electron. Conf.*, 2006, pp. 38–44.

[8] P. S. Shenoy et al., "Automatic current sharing mechanism in the series capacitor buck converter," in *Proc. IEEE Energy Convers. Congr. Expo.*, 2015, pp. 2003–2009.

[9] B. Oraw and R. Ayyanar, "Small signal modeling and control design for new extended duty ratio, interleaved multiphase synchronous buck converter," in *Proc. IEEE 28th Int. Telecommun. Energy Conf.*, 2006, pp. 1–8.

[10] B. Oraw and R. Ayyanar, "Large signal average model for an extended duty ratio and conventional buck," in *Proc. IEEE 30th Int. Telecommun. Energy Conf.*, 2008, pp. 1–8.

[11] Y. Chen et al., "Virtual intermediate bus CPU voltage regulator," *IEEE Trans. Power Electron.*, vol. 37, no. 6, pp. 6883–6898, Jun. 2022.

[12] M. Faccio, G. Ferri, and A. D'Amico, "A new fast method for ladder networks characterization," *IEEE Trans. Circuits Syst.*, vol. 38, no. 11, pp. 1377–1382, Nov. 1991.

[13] D. H. Zhou, A. Bendory, P. Wang, and M. Chen, "Intrinsic and robust voltage balancing of FCML converters with coupled inductors," in *Proc. IEEE 22nd Workshop Control Model. Power Electron.*, 2021, pp. 1–8.

[14] M. Chen and C. R. Sullivan, "Unified models for coupled inductors applied to multiphase PWM converters," *IEEE Trans. Power Electron.*, vol. 36, no. 12, pp. 14155–14174, Dec. 2021.

[15] P. Wang, D. Zhou, Y. Elasser, J. Baek, and M. Chen, "Matrix coupled all-in-one magnetics for PWM power conversion," *IEEE Trans. Power Electron.*, vol. 37, no. 12, pp. 15035–15050, Dec. 2022.

[16] Z. Ye, Y. Lei, Z. Liao, and R. C. N. Pilawa-Podgurski, "Investigation of capacitor voltage balancing in practical implementations of flying capacitor multilevel converters," *IEEE Trans. Power Electron.*, vol. 37, no. 3, pp. 2921–2935, Mar. 2022.